crystals

MDPI

Article

Microstructure and Properties Variation of High-Performance Grey Cast Iron via Small Boron Additions

Grega Klančnik [1,*], Jaka Burja [2], Urška Klančnik [3], Barbara Šetina Batič [2], Luka Krajnc [1] and Andrej Resnik [4]

[1] Pro Labor, d.o.o., Podvin 20, SI-3310 Žalec, Slovenia
[2] Institute of Metals and Technology, Lepi pot 11, SI-1000 Ljubljana, Slovenia
[3] Valji d.o.o., Železarska Cesta 3, SI-3220 Štore, Slovenia
[4] Omco Metals Slovenia d.o.o. Cesta Žalskega Tabora 10, SI-3310 Žalec, Slovenia
* Correspondence: grega.klancnik@prolabor.si

Abstract: A study was undertaken to investigate the effects of small boron additions on the solidification and microstructure of hypo-eutectic alloyed grey cast iron. The characteristic temperatures upon crystallisation of the treated metal melt were recorded, specifically those concerning small boron addition by using thermal analysis with the ATAS system. Additionally, a standardised wedge test was set to observe any changes in chill performance. The microstructures of thermal analysis samples were analysed using a light optical microscope (LOM) and field emission scanning electron microscopy (FE-SEM) equipped with energy dispersive spectroscopy (EDS), which reveal variations in graphite count number with the addition of boron within observed random and undercooled flake graphite. The effect of boron was estimated by the classical analytical and statistical approach. The solidification behaviour under equilibrium conditions was predicted by a thermodynamic approach using Thermo-Calc. Based on all gathered data, a response model was set with boron for given melt quality and melt treatment using the experimentally determined data. The study reveals that boron as a ferrite and carbide-promoting element under the experimental set shows weak nucleation potential in synergy with other heterogenic nuclei at increased solidification rates, but no considerable changes were observed by the TA samples solidified at slower cooling rates, indicating the loss of the overall inoculation effect. The potential presence of boron nitride as an inoculator for graphite precipitation for a given melt composition and melt treatment was not confirmed in this study. It seems that boron at increased solidification rates can contribute to overall inoculation, but at slower cooling rates these effects are gradually lost. In the last solidification range, an increased boron content could have a carbide forming nature, as is usually expected. The study suggests that boron in traces could affect the microstructure and properties of hypo-eutectic alloyed grey cast iron.

Keywords: boron; cast iron; solidification; thermal analysis; Thermo-Calc

Citation: Klančnik, G.; Burja, J.; Klančnik, U.; Šetina Batič, B.; Krajnc, L.; Resnik, A. Microstructure and Properties Variation of High-Performance Grey Cast Iron via Small Boron Additions. *Crystals* **2024**, *14*, 103. https://doi.org/10.3390/cryst14010103

Academic Editor: Shouxun Ji

Received: 28 December 2023
Revised: 14 January 2024
Accepted: 17 January 2024
Published: 22 January 2024

1. Introduction

The nucleation and growth of graphite is complex. Based on Stefanescu et al. [1], the graphite aggregates in iron–carbon melts crystallise via hexagonal faceted graphite platelets, and impurities (O, S, etc.) inside the metal melt may change the graphite growth considerably by affecting the thickening mechanism of the graphene sheets. The impurities and formed nuclei can affect graphite morphology and shape considerably. Oxides (MgO, AlO); nitrides and carbo–nitrides ((Ti, Zr)(C, N), AlN, (Mg, Si, Al)N, TiN etc.); sulfides (MgS, (Mg, Ca)S, MnS, etc.); phosphides ((Mg, La, Ce)P); sulpho-oxides (Mg, Ca(SO), etc.); or complexes between all of them are all considered for potential nuclei [1–4]. Based on Sommerfeld et al., [3] MnS precipitates are preferred sites for graphite nucleation in iron cast melts based on investigations done on EN-GJL-200, but the temperature for MnS formation changes in relation to the melt chemical composition, for example with the addition of Ti and resulting Ti–carbo–sulfides, which deplete sulphur in the melt needed for MnS

formation at higher temperatures. Based on Stefan et al. [5], complex second compound nucleates on manganese sulfides (Mn, X)S are found for graphite nucleants, where X = Mg, Ca, Sr, Al; all in sizes under 10 μm. It is notable that oxy-forming elements, such as Mg, improve the (Mn, X)S graphite nucleation by forming a thin superficial layer as oxide or oxy-sulfide. This is presumably due to a better crystallographic compatibility compared to purely sulfide with cubic system. According to Campbell [6], mostly liquid oxide films (bi-films) of different compositions based on SiO_2 act as substrates for nucleation of oxy-sulfide nuclei and the growth of flake and nodular graphite. In the case of boron, which is commonly used for white irons, liquid borates are expected to form. Based on Campbell [6] liquid iron–borate can form, preventing oxide formation substrates for graphite growth. Which exact type of M_xB_Y will form is related to the melt composition. However, boron is an element with an affinity to oxygen, potentially forming oxy-sulfides as well as nitrides. It seems that B_2O_3, if formed, is not considered to be a highly stable oxide based on a Richardson–Ellingham diagram, as shown later in the paper. Based on [7–9], boron, in combination with Cr, affected carbide and boride formation significantly in white cast iron and high-speed alloy steels. Boron in traces inside different systems is considered as infinite dilution [10]. It can also be considered as an impurity in some cases. Based on the same assumption, relationships that are close to linear are expected and therefore also observed in this study.

Data in the literature regarding the effects of boron in cast irons identifies boron as an influential and strong carbide stabiliser and ferrite-promoting element; therefore, it is an element that has the potential power for affecting the matrix hardness (with boric pearlite, etc.) and overall hardness. The formed boron complexes are commonly described as α-Fe + Fe_3C + Fe_2B. It is also recognised that certain elements, such as Sr and Sb can enhance the hardness of pearlite; therefore, the effects of boron can be expected to be balanced with certain inoculation/elemental additions. It is recognised that time—and an additional quantity of inoculants—effects the microstructure and hardness in lamellar graphite cast irons [11]. For example, by the microalloying in the grey lamellar iron with simultaneous phosphorous and boron (P + B), the micro-abrasive wear was studied where increasing hardness of pearlitic matrix and refined interlamellar spacing was noticed [12]; however, it is not clear how much this was contributed by the boron addition.

A hardness increase in chill is possible due to the formation of a carbide network. The potential hardness drop can also be expected with the addition of boron due to ferrite promotion, but it is possible to counteract with N and Ti on high-strength GJS [13,14]. These responses are usually not comparable overall, despite the fact that an overall average hardness increase is mostly expected with boron for grey iron. However, it was also shown that hardness decrease can also appear after exceeding a certain boron limit. This limit of different material behaviour seems to vary considerably with different iron grades. This is potentially related to synergistic effects with other active-forming elements, such as the aforementioned Ti and N. The boron effect is potentially sensible also to CEQ. As boron is recognised as a ferrite stabiliser—and this could be unwanted for pearlitic grades but beneficial for grades which are aimed to be mainly ferritic in the final condition (as ductile GJS types). However, chill with an excessive presence of carbide network should be avoided. In the case of Keivan, et al. [15] no considerable change in graphite size with boron was noticed up to 131 ppm of added B for GJS type on different thickness sections, but the effect was visible as a change in ferrite content. Similarly, no change in distribution and number density of graphite nodules was noticed by Bugten, et al. [16] up to 130 ppm B. In the case of certain ductile irons, the boron seems to degrade the graphite sphericity towards compacted (vermicular) graphite and degrades the needed mechanical properties compared to nodular/ductile irons. The degradation of mechanical properties is also partially the result of primary carbide precipitation. This also seems to be valid for thicker sections. However, it seems that this boron response is not always consistent, as shown in the patent and in [13,16,17], where boron in ductile iron minimises the dissolved nitrogen in the molten iron by estimating that BN were formed and are potentially working as

new heterogeneous nuclei for graphite precipitation, consequently increasing the nodule count, promoting the ferrite content, diminishing the nitrogen effect on carbide stability and affecting the stability of pearlite during annealing. This was achieved by setting the optimal boron content [15,17].

In some cases, excessive boron (>200 ppm B) for plain grey cast iron presumably promotes B-type and D-type graphitic structures, therefore decreasing tensile strength over certain boron limits. The effect of boron on annealing is quite contradictory, as boron can work as a graphite promoter in the case of malleable irons by promoting temper carbon from carbides, and it also works as a carbide stabiliser in white cast irons for increasing wear and—in some cases, such as for nodular—improves the carbide's annealing stability. Based on shorter diffusion paths due to higher nucleation graphite count, the annealing ability could also be improved [18–21].

It is recognised that boron narrows the eutectic region between stable (EG) and metastable solidification (EC); $\Delta T_E = T_{EG} - T_{EC}$, along with V, Cr, Mn, Ti, and Mo. The intensity of the ΔT_E change is also related to the distribution coefficient of elements between cementite and austenite, as with other elements, and is therefore dictated by the actual solidification rate [22]. Interestingly, a controlled addition of boron and nitrogen can also have a positive effect on the control of heavy grey iron castings by the potential formation of boron-based nuclei for graphite growth. However, the actual presence of BN has not yet been confirmed [23].

Based on the above, boron appears to be a sensible element, and sensibility rises with boron content. When added intentionally, the elemental yield varies, but when boron is already in the scrap or iron, the boron is fully preserved (high yield). When boron is entrapped in the metal melt it can have an important influence on the quality of produced as-cast irons and on annealed grey irons [19,20,24]. The literature shows that boron can promote heterogeneous graphite distribution, variations in mechanical properties after it exceeds certain limits and that interactional effects with other elements are also possible.

In this study, an alloyed grey cast iron is considered instead of plain cast iron for testing the interactions with intentionally added boron during solidification. The boron in this study is highly limited and the limitation is set from the measurements established under industrial environments where boron is considered as contaminant.

2. Materials and Methods

The chemical composition was controlled by using the starting non-boron (unmodified) cast iron used for remelting to have repeatable behaviour during solidification. This would also help to achieve repeatable chemical composition (which was taken as the reference material further in this paper). The tight elemental control is important for controlling the starting eutectic solidification interval (freezing) and to observe the main target factor considered as a single factorial test, namely the boron influence. Additionally, the temperature profile, furnace reheating, maximum allowable temperatures, time of melting and casting temperatures were carefully controlled for maximising the repeatability of the tests. The melting was carried out in an open-air induction furnace equipped with a furnace isolative lid for Ar surface purging to minimise slag formation. The inner wall of the high-frequency furnace was made of MgO-based refractory. The unmodified material was cut into smaller pieces within similar melting and tapping times and surface-to-volume ratios for comparable oxide entrapment via surface contaminants that potentially also work as nuclei (affecting active carbon equivalent, ACEL). Secondary remelting of the starting non-boron grey iron can help improve the chemical homogeneity of prepared final melts. For sufficient and repeated inoculation, FeSi(low Al) was used in all cases (approx. 0.4 wt.%) to promote repeatable starting heterogeneous nucleation sites. The time interval between FeSi addition and first tapping is 5 min. The primary melt treatment was already carried out in the induction furnace just before tapping into the well-preheated graphite ladle. It was then cast into the Thermal Analysis cell (TA) and wedge (chill) cells with and without boron, in this order. In the case of TA, all pourings are made without the

addition of strong carbide forming tellurium, as this was done before the test to observe the suitability of the equations used in this study for white solidification temperature prediction ($T_{EC} = T_{Metastable}$). No additional chill was allowed for TA or the wedge. As a tool for analysing the recorded solidification nature, ATAS MetStar tool (Nova Cast, Ronneby, Sweden) was used. Microstructural observation on prepared metallographic samples was done by ImageJ (National Institutes of Health, USA) [25] (https://imagej.net/). The maximum field for graphite count detection per image was 1027 µm × 1369 µm. The FeB additions were introduced as a fine powder by small additions in both mould cavities of the TA cell and wedge cell to maximise the boron yield. The yield was not constant; therefore, all boron values are represented only as measured ones. The experimental setup is presented in a way that observes the short-time inoculation effect (last moment "in-mold" inoculation), if it exists with the addition of boron, as suggested in the literature. In the case of TA, the samples were extracted just under the thermocouple junction to have representative values coupled with the TA data.

The wedge cavity was prepared with dry silica sand and by using a special 3D-printed core, as shown in Figure 1a. For TA analysis, in Figure 1b, a regular TA cup (Nova Cast, Ronneby, Sweden) was used equipped with a K-type thermocouple calibrated within ±1.2 °C at 1000 °C [26].

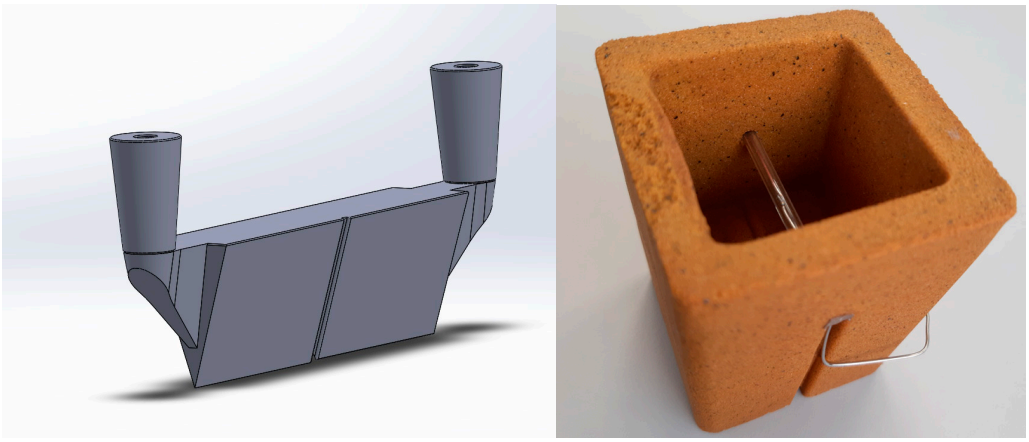

(**a**) (**b**)

Figure 1. An example of (**a**) the 3D model for wedge test with the feeder design used for the 3D printed single core for sand mould preparation to be used for chill tendencies observations after solidification. (**b**) ATAS cup.

The hardness of the TA analysed samples was measured using the Brinell method, with a 2.5 mm tungsten carbide indenter and a 187.5 kg load (HBW 2.5/187.5) (based on ISO 6506-1 [27]), measured on metallographically prepared samples. The microstructure was observed using metallographic samples in unetched conditions using a Light optical microscope (Olympus DP70 LOM, Tokyo, Japan) and FE-SEM (Zeiss CrossBeam 550, EDAX Octane elite EDS detector, Oberkochen, Germany). Using FE-SEM, the focus was on both the inclusions and boron in the inclusions. The microstructure using LOM was evaluated by regular standards, such as ISO 945 [28].

The thermodynamic prediction was made by Thermo-Calc (Thermo-Calc 2017a, TCFE8, Sweden). For the estimation of physical properties, JMatPro 6.1 (Sente Software Ltd., Guildford, UK) was used. The input data for the calculations was performed with a chemical composition based on optical emission spectrometry (ARL 3460, ThermoFisher Scientific, Waltham, MA, USA) and LECO for sulphur and carbon determination (LECO CS-600, Leco Corporation, St. Joseph, MI, USA). For nitrogen and oxygen LECO TC436 (Leco Corporation, St. Joseph, MI, USA) was also used. The boron measuring limit was set under 5 ppm.

Figure 1a, above, depicts the 3D model of the wedge test specimen, which adheres to the geometry prescribed in standard test method A, W4 [29], while Figure 1b shows a photograph of the measuring ATAS cup (cell) from Nova Cast [26].

The results of the wedge test (W4) and TA were primarily correlated with the measured boron content based on linearity. The search for a correlation between chill and pouring temperatures and related superheat (difference between pouring temperature and liquidus temperature) was included to observe if temperature control was sufficient for the observation of boron influence as a single factorial test. For this purpose, Pearson's correlation coefficient (r) was calculated where +1 or −1 reveals a perfect positive and negative correlation between the measured variable (y) and, for example, the measured boron variable (x). If r is under the absolute value of ±0.30 (a rule of thumb) or close to 0, no linear correlation is observed. The data of linear and nonlinear regression for the observed population were evaluated by the R^2 coefficient (coefficient of determination), and if R^2 is 1, then the fit is perfect. The statistical significance of r (assessed by the calculated p-value) was also calculated for each potential linear relationship between variables. A statistical significance was established with 0.05. When the p-value was less than 0.05 (critical level of significance), then the null hypothesis (H_0) was rejected (no linear relationship between the two variables with $r = 0$), and an alternate hypothesis was accepted (there is a relationship between variables), based on the model presented in [30–32]. If the p-value is under 0.01, then the response is considered very significant.

3. Results and Discussion

3.1. Chemical Composition

The measured chemical composition is given in Table 1. The basic composition is set for flake graphite formation. The flake structure is intended for the studied special grey iron at elevated temperatures. A higher content of carbide stabilisers can also be recognised in Table 1 (Cr, Mo, V, Ti) for increased wear and temperature stability. For this study, boron as a contaminant is also included. The chemical composition was kept stable for a stable carbon equivalent control (CEQ), and its counterpart carbon equivalent was also evaluated through liquidus (CEL, ACEL). The carbon content was relatively low to provide evidence of the potential chill effect with the boron additions. The CEQ was preserved as a fixed value, as the boron effect can vary with CEQ due to the changed graphitisation ability, according to [18]. The Si value represents the final inoculated value, as the final chemical composition is treated with FeSi before boron interactions with the melt and performed TA. The nitrogen, possibly also affecting chill as a carbide stabiliser [17], is controlled in the range 85–100 ppm range and is regarded as reasonable. The nitrogen pickup from scrap, alloys and the atmosphere was under control [33].

Table 1. The chemical composition of melts is based on the extracted TA samples. The values are gathered and referred to as OES and LECO (in wt.%) values. Boron, nitrogen and total oxygen are in ppm.

	C	Si	Mn	Cr + Mo	Ti + V	Ni + Cu + Co	$[O]_{tot}$	B	N	CEQ *
	3.22	2.22	0.57	0.60	0.13	0.78	33–71	0	94	3.77
								19	85	
								30	100	
								37	97	
St.dev.	0.01	0.05	0.01	0.01	0.01	0.07	15	/	6.48	0.02

* CEQ = CEL = %C + %Si/4 + %P/2.

In Table 1 standard deviation of basic composition between heats are given, with boron as an exception.

3.2. Thermodynamic Approaches

A thermodynamic equilibrium prediction of the temperature-related phase evolution, using Thermo-Calc, was established to clarify the potential synergy of the boron with other elements under equilibrium conditions. The Diamond_FCC_A4 and Cementite were suspended for stable prediction of phase evolution versus temperature. The gas phase was allowed for the same calculations. The typical diagram of phase evolution concerning temperature is shown in Figure 2. Based on such diagrams, characteristic temperatures were gathered and presented in Table 2. When adding boron, a change is predicted in decreased solidus temperature ($T_{solidus}$), as shown in Table 2.

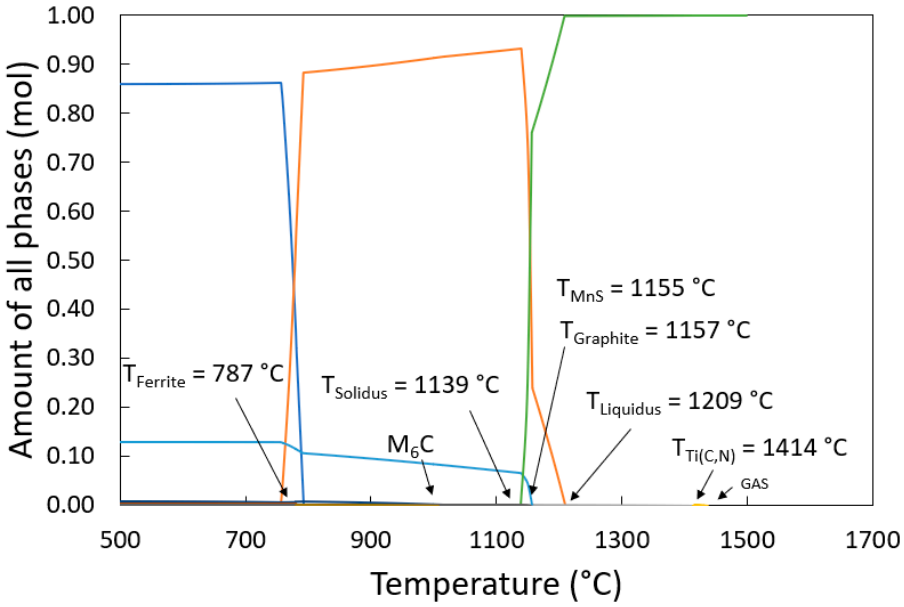

Figure 2. An example of equilibrium phase evolution in relation to temperature. A reference alloy without boron (untreated sample: 0 ppm B). When boron is added M_3B_2 is stable (Table 2). Calculation: Thermo-Calc (TCFE8).

Table 2. Predicted characteristic temperatures determined by the Thermo-Calc (TCFE-8) calculation (in °C) by fixed nitrogen content of 100 ppm and 150 ppm.

B (ppm)	N (ppm)	Ti(C, N)	Austenite	Graphite	MnS	$T_{solidus}$	M_3B_2	M_6C	MC	Ferrite	MC_Eta	BN
0	100	1414	1209	1157	1155	1139		1014	1005	787	774	No
19	100	1414	1208	1157	1155	1087	1087	1013	1008	787	774	No
30	100	1414	1208	1157	1155	1087	1088	1010	1008	787	774	No
37	100	1414	1207	1157	1155	1087	1088	1008	1008	787	774	No
37	150	1414	1207	1157	1156	1088	1087	1013	995	786	774	1125

Based on Table 2, there is no expected precipitation of BN for given compositions (0–37 ppm B and 100 ppm N) and, therefore, boron is not expected to work as a potential inoculator based solely on the presumption of formed BN. The only nitride or carbo–nitride that are present before the primary and eutectic austenite and eutectic graphite start to precipitate from the liquid is Ti(C, N) or co-precipitated $(Ti, V, Fe)_1(N, C, Va)_1$. Based on these calculations, when nitrogen is sufficiently raised, BN seems to be thermodynamically stable, but the formation of BN is predicted to occur after graphite precipitation. Therefore, up to 150 ppm of raised nitrogen (N) the BN seems not to be present as a major active nucleator for graphite precipitation. However, the precipitation of BN is still predicted above the solidus temperature, which gives it the possibility of being a weak inoculator in the last solidification region. The BN is formed at 1125 °C at 37 ppm B at raised nitrogen,

and is also potentially in the form of solute enrichment in the last liquid region. According to the calculations, when boron is included, it is integrated into the graphite phase from start at approx. 1157 °C, and boron content rises to approx. 1086 °C. This is the temperature where M_3B_2 starts to become stable. Manganese sulfides (MnS), as non-metallic inclusions, are also predicted and expected in the last solidification region. The potential complexes formed between iron–molybdenum based M_3B_2 and MnS are not excluded due to their thermodynamic co-existence, and this is also the case for Ti(C, N), which is formed in the early stage of solidification. Based on the predicted equilibrium solidification, carbides (M_6C, MC is also interpretated as M(C, N) type, etc.) are not formed from the liquid phase; however, under actual non-equilibrium conditions, primary carbides can be found, as shown later in this study.

Based on the measured chemical composition, shown in Table 1, the activities of carbon in the liquid phase versus boron can also be calculated. The carbon activity predictions are carried out by first calculating the activity coefficient of carbon (f_C). The calculation is made with the presumption of dilute solutions by first incorporating the Henryan activities (using 1 wt.% alternative reference state) in a multi-component liquid system to describe the thermodynamic behaviour of element (C) by first-order interaction parameters (coefficients) of carbon (e_i^j, where i = C and solute j = Si, Mn, B etc.). The protocol and interaction values for this calculation are found elsewhere [34]. The carbon activity using the Raoultian reference scale, $a_{C\ (R)}$, in liquid is preferred and recalculated from the Henryan scale. The carbon activity values reveal practically no obvious activity changes with such a small boron content, toward the ability to graphite/carbide formation; $a_{C(R)}^{o\ ppm\ B} = 0.356$ and $a_{C(R)}^{100\ ppm\ B} = 0.358$. The calculated values using the CALPHAD approach reveal similar values ($a_{C(R)}^{0-37\ ppm\ B} = 0.381$) concerning boron for carbon activity in liquid, and these values are similar to the values for stable pseudo-Fe-C system (ternary Fe-C-Si) for given carbon and silicon content [35–37]. However, by increasing the boron content, the carbon activity gradually increases. An increase in the activity of carbon in liquid reveals an improved ability for carbon to separate as graphite in the Fe-C system [38]. However, based on the diagram below, Figure 3, the temperature difference between stable and metastable eutectic intervals is barely noticeable for a given boron interval, but a higher boron content reveals a weak tendency toward mottled or white solidification if the content of boron is sufficient. This is possible when elemental enrichment appears in the last solidification front. In this study a low superheat was obtained to limit any elemental enrichement. However, in the case of added nitride forming Ti, as in our case, a graphitising influence can also be promoted among carbide promotion, as it is related to the nitrogen levels achieved in the melt [38]. This indicates a complex graphitisation behaviour for a given composition.

3.3. Wedge Test

After pouring the melt into the wedge cell and letting it cool to ambient temperature, the test chill specimen was broken in half to observe the fractured topography, as seen in Figure 4. An obvious difference in chill is observed within the heats. The measured data is given in Table 3. For the wedge test, according to test method A, the evaluation is carried out according to standard procedure [29]. As it is recognised by the standard A367, the amount of chill is strongly affected by the pouring temperature. The recorded pouring temperature was also controlled at its best by having the same melting loads (melt enthalpy capacities) and similar temperature profiles from melting to pouring. The maximum melt temperature before pouring was up to 1310 °C. A linear correlation was observed between the measured maximum pouring temperatures with measured clear chill depths measured by the width, W, ($r = -0.92$). However, a linear regression of the data indicates that the pouring temperature is outside measurable significance (p-value = 0.08, $R^2 = 0.845$), especially when compared with the boron measured values with W values. A close-to-linear trend was established for the measured boron values on wedge samples with measured clear chill (with p-value = 0.038, $R^2 = 0.924$). However, according to statistics,

the change due to boron is regarded as significant instead of very significant. It should be emphasised that, based on the data, synergistic effects could be possible between boron and the pouring temperature (and related superheat), but in the current study, multilinearity for the same observed parameter was not observed.

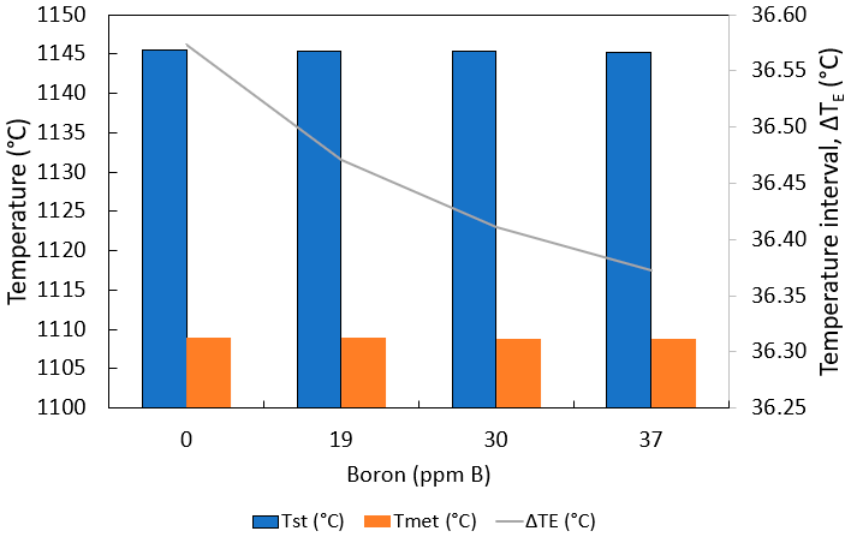

Figure 3. Effect of boron on eutectic solidification region defined by $T_{EG} - T_{EC}$ and calculated based on equations [22,38,39] reveals that boron is in function of a weak carbide stabiliser decreasing T_{Stable} and $T_{Metastable}$. The intensity is related to actual boron distribution in the last solidification front. The theoretic temperature difference (ΔT_E) between both eutectics for the studied melts is practically negligible.

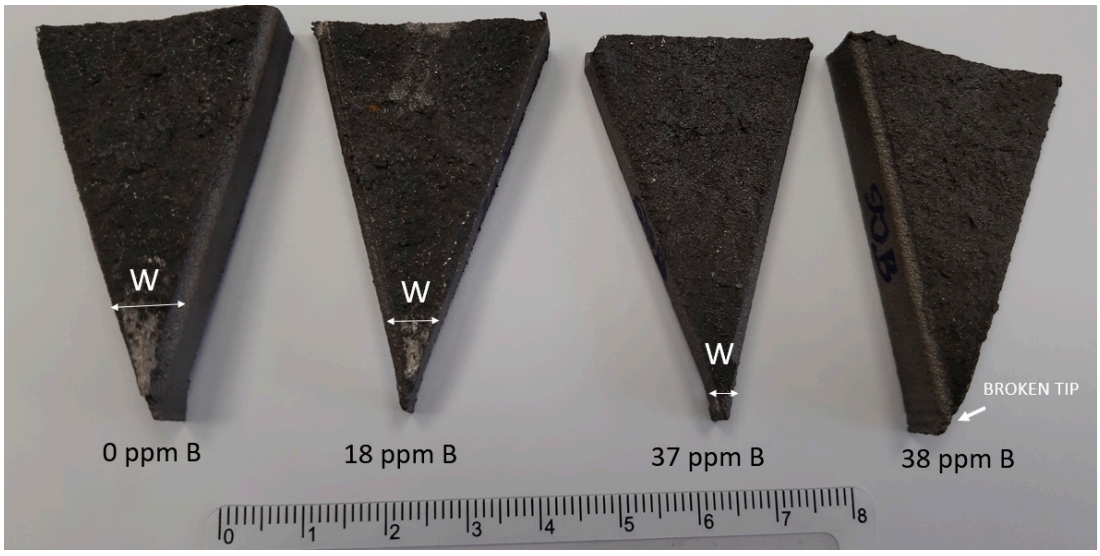

Figure 4. Decreased chill (*W*) with the addition of boron is obvious. The dark grey appearance of the majority of the sample's cross-section reveals the overall effective melt inoculation treatment (by also including FeSi). No macro-porosity was observed in the cross-sections.

Table 3. Clear chill boundary measured from the apex to the starting of the second (mottled) zone (in mm) with the measured boron content. More in [29].

Boron (ppm B)	**0**	**18**	**37**	**38**
W	10.98	9.60	3.45	<3.45 *

* The tip edge is broken therefore the *W* is not reliably measured.

3.4. Thermal Analysis (TA)

Based on the recorded (temperature–time) cooling curves, several parameters were extracted to evaluate basic information about the melt behaviour [39]. The basic parameters are T_{Liq}, T_{ELow}, T_{EHigh}, T_{ES}, T_{Sol}, *Rec*, *UQ*, *ACEL*, *S1* and *GRF2*, and these are interpreted as liquidus temperature; the temperature of eutectic undercooling; the temperature of eutectic recalescence; eutectic start; solidus temperature (a solidified structure is represented with grey in Figure 5); recalescence (defined as $T_{EHigh} - T_{Elow}$, the rise of temperature due to graphite precipitation); undercooling quotient; active carbon equivalent (calculated from T_{Liq}); relative amount of primary austenite precipitation (yellow region in Figure 5); and first derivate of the cooling curve at solidification finish (graphite factor number 2), respectively. GRF2 is also a measure for inverted heat conductivity in a solid, being important for the purposes of graphite quantity and shape [40]. In this paper, the sign *Rec* is used for recalescence and the small letter *r* for the Pearson correlation coefficient, to avoid confusion.

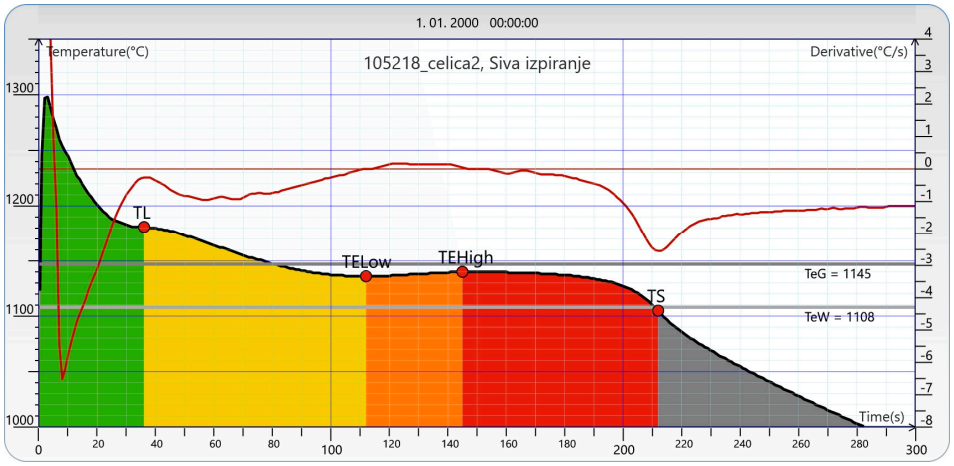

Figure 5. An example of an ATAS analysed cooling curve with the first derivate, revealing the hypothetic solidification nature of the investigated alloyed grey iron. Sample: 37 ppm B. Color explanation: Green—Liquid phase, so-called superheat (between $T_{pouring}$ and $T_L = T_{Liq}$), Yellow—S1 (between T_{Liq} and T_{ELow}; precipitated as pro-eutectic austenite), Orange—S2 (between T_{E*Low} and T_{EHigh}; Eutectic region No.1), Red-S3 (between T_{EHigh} and $T_S = T_{Sol}$; Eutectic region No.2) and Grey ($< T_{Sol}$; solidified as-cast structure).

An automated ATAS system was used for analysing the recorded solidification curves of the non-boron and boron-treated samples. Instead of using a TA cup with Te seed promoting white solidification, an equation based on reference [22] is used instead, which also includes the (soluble) boron influence. Similar equations are valid for stable (graphite) solidification. Based on the temperature interval between stable (grey) and metastable (white) eutectics, the basic melt characteristics were observed using the ATAS system, as shown in Table 4. All samples are hypo-eutectic based on the calculated constant CEQ, with 3.77 and active carbon equivalent (*ACEL*) changes from batch to batch, as observed by *ACEL* [25]. The evidenced primary austenite precipitation suggests the possibility of forming D and/or E graphite distribution (according to EN ISO 945 [28]). In the case of a higher *ACEL*, a transition towards A distribution is possible with potential locally thicker flakes due to high eutectic temperatures obtained by TA. The ACEL increases on average with boron-contaminated samples (approaching the eutectic region with C ≈ 4.3%) but with no obvious correlation. The relevant austenite precipitation index (*S1* region, the yellow area in Figure 5) is estimated to be rather similar, and with the highest values for the non-boron heat equivalent, with 43.68% of the primary austenite compared to lowest values of 41.71% within boron treated heat. The overall increase of eutectic graphite (based on *ACEL*) is observed on boron-treated samples, but the trend is non-linear as the data are scattered. The results reveal that boron contamination with values up to 37 ppm B and its

effects on chill or graphitisation are not straightforward. The data also reveal the usefulness of using TA during the melt quality check (like *ACEL*) when preparing the melt with scrap, instead of simply relying on the chemical composition and related CEQ.

Table 4. Measured parameters by using ATAS. The boron values are the measured boron contents in TA samples. T_{Stable} = 1145 °C and $T_{Metastable}$ = 1108 °C are calculated by [22,39] and ACEL by [38,41].

Internal Name	ppm B	T_{Liq}	T_{ELow}	T_{EHigh}	T_{ES}	T_{Sol}	*Rec*	UQ	ACEL	S1	GRF2
102130_1	0	1186	1127	1133	1166	1089	6	1.0	3.89	43.68	58
105218_1	19	1181	1136	1141	1163	1108	5	1.2	3.94	42.86	46
102130_2	30	1184	1130	1134	1169	1095	4	1.5	3.91	41.71	58
105218_2	37	1181	1136	1140	1168	1105	4	1.5	3.94	43.44	52

ACEL = $14.45 - 0.0089 \cdot T_{liq}$ [38,41].

There is one measurable relation with boron independent of *ACEL* (related to T_{Liq}), and this is recalescence, *Rec* ($Rec = T_{EHigh} - T_{ELow}$). It is agreed that inoculation reduces eutectic undercooling [41], and that this can be observed by the undercooling quotient here described as *UQ* (Equation (1)). The $Rec_{Reference}$ in Equation (1) stands for recalescence of untreated (0 ppm B) heat and Rec_{Boron} related eutectic undercooling measured for boron-added melts:

$$UQ = Rec_{Reference} / Rec_{Boron} \quad (1)$$

Based on the *UQ* values in Table 4, where the *UQ* increase indicates possibly the eutectic cell number change, it is clear that the change regarding boron can be described as having a weak inoculation phenomenon only. This is also true when considering that T_{sol} is higher for boron-treated melts (contrary to predictions, Figure 2). This reveals that boron is an important element, even in traces, during the production, as well as for special grey iron melts. It is notable that, for a given laboratory set, the recalescence or, more importantly, *UQ*, stops at values of 30 ppm B, and could indicate an achieved maximum allowable inoculation for a given laboratory set. It should be remembered that this inoculation must be a synergy of boron complexes with already present nucleation sites (from scrap, added FeSi, etc.) or, as shown by Thermo-Calc, partially related to the composition itself.

The liquidus temperature somehow decreases with the boron content for special cast iron grades and, therefore, the added boron did not act as a nucleus for primary austenite crystallisation, according to measured data. Additionally, the graphite eutectic and solidus temperatures are higher than the reference indicating small changes in the solidification paths. Overall increased solidus reveals that, compared to the reference (of non-boron) sample, the tendency to segregations and related chill was decreased. This is similarly the case for T_{ELow}. The measured effects using TA are the opposite of those found in Pawaskar's study [18], and this is consistent with the observed wedge specimen depth change with boron in this study. The closing of the solidification interval between liquidus and solidus is interesting, and similar to observations for plain cast irons in reference [18,19]. A higher nucleation potential for given heats, compared to plain cast grey irons, can be expected, and this is present due to a probable nucleus formation based on pre-existing nitrides. It is also interesting that the non-calibrated eutectic cell count (ECC) was followed under slow solidification rates, and no obvious ECC correlation with boron was observed, as it was not obvious with the measured graphite count. This is despite the higher counts observed for the highest boron content, as shown in Figure 6. This reveals that an obvious graphitisation effect was not achieved and confirmed during slow cooling rates, as it was significant for the wedge test.

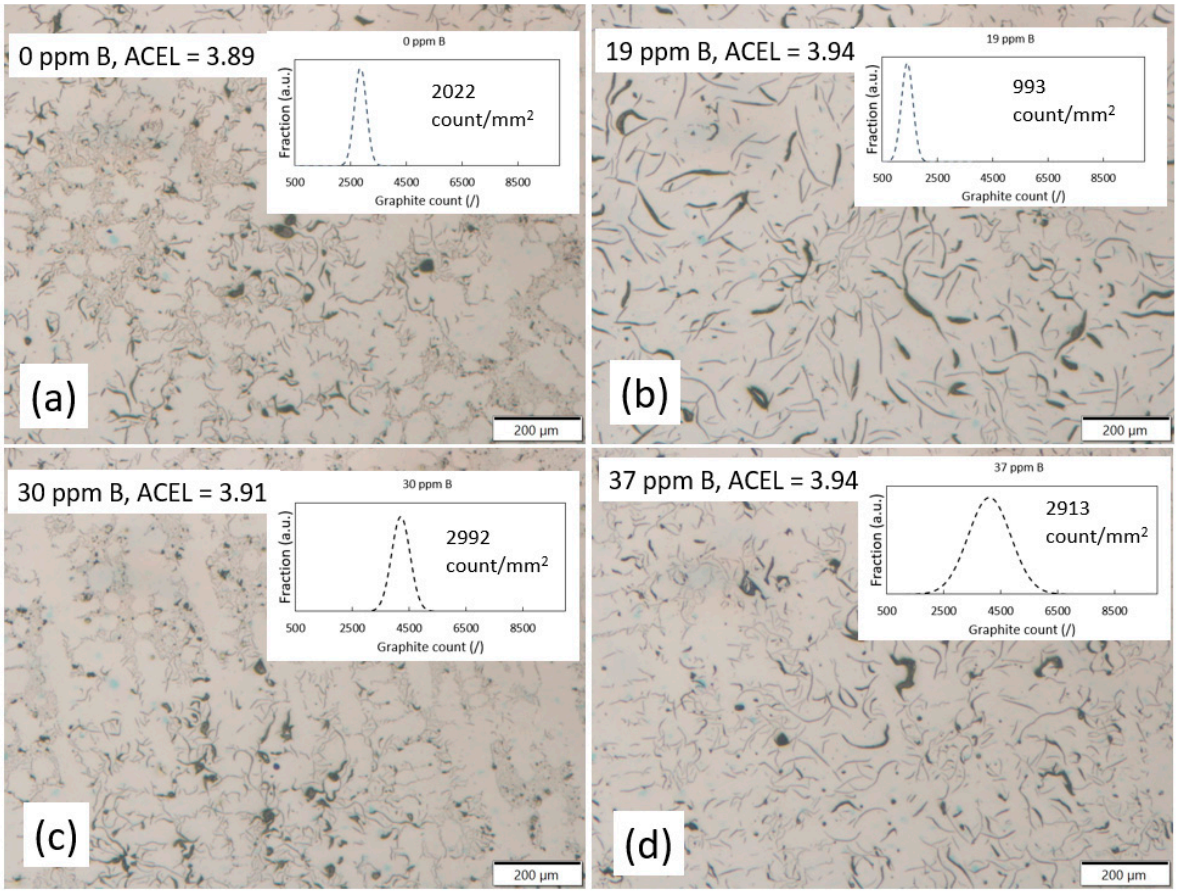

Figure 6. An example of the as-cast structure of TA samples and related graphite count distribution (**a**) 0 ppm B with finer size D/E graphite as reference (1 sigma, min–max = 2630–3058); (**b**) 19 ppm B with D/E graphite with thicker graphite flakes inside the eutectic cells of A as the majority (1 sigma, min–max = 1186–1606); (**c**) 30 ppm B with D/E with finer and local coarse size inside the eutectic cells (1 sigma, min–max = 3884–4531); (**d**) 37 ppm B with D/E with thicker eutectic flakes of A as the majority (1 sigma, min–max = 2995–5197). Calculated *ACEL* [41] from the obtained T_{Liq} is between 3.89 and 3.94. Enlargement: 50×. State: Polished.

3.5. Thermal Conductivity

Thermal conductivity is an important physical property for elevated temperature use. The increased fractions of transformed austenitic primary crystals and branched D-type graphite lower the ability to transfer heat and are related to achieved cooling rates, inoculation efficiency, etc., meaning that it is not simply related to basic nominal composition [40]. A higher content of A-type is usually desired where high thermal conductivity and low friction losses are needed [23]. Thermal conductivity was not directly measured at room temperature. However, it is estimated by using the indirect method by observing the end of the solidification curve during TA, which can indicate the graphite shape. In this case, the angle of the derivate marked as GRF2 was used, as shown in Table 4. According to Stefanescu et al. [39], low angles can correspond to increased thermal conductivity. Compared to the analysed boron content and GRF2, no linear trend with thermal conductivity was observed ($r = -0.23$, $R^2 = 0.05$). The lowest angles (highest conductivity) were determined with the sample with the highest *ACEL*, regardless of the boron content (19 and 37 ppm B). This complements the improved graphite distribution uniformity observed in Figure 6. In the case of the sample with the lowest *ACEL*, the undercooled dendritic graphite indicates lower heat transfer ability, even if graphite count is increased (compared to 0 and 30 ppm B with GRF2 and graphite count). Carbides have

an influence on the conductivity, but the fractions are comparable with the TA samples, as shown under FE-SEM investigation later.

An example of estimation of thermal conductivity for a stable reference sample with ferritic–pearlitic matrix and lamellar type of graphite is between 48 and 35 W/mK for 25 and 500 °C, respectively. Boron within the given limits is considered, based on GRF2, as non-significant to thermal conductivity values. Based on prediction (using the JMatPro 6.1, internal database: General physical properties,) the thermal conductivity is close to linear with the increased working temperature.

3.6. Microstructure

3.6.1. LOM

Despite having the same carbon equivalent (CEQ), the microstructures of the TA extracted samples (taken from the centre of the measuring cup) differ considerably in terms of their slow solidification rate, as shown in Figure 6. According to ATAS, the calculated *ACEL* from measured T_{Liq} identify the actual changes observed from batch to batch and goes well with the formed microstructure. A higher *ACEL* brings about a combination of A and D graphite types, with a majority of A (compare sample with 19 ppm B and 30 ppm B), instead of mostly D/E type of (undercooled/dendritic) graphite. This shows that actual achieved *ACEL*, as a measure for the achieved melt quality, prevails for the given samples compared to small boron content for microstructure evolution. This microstructure evolution stands for the absolute cooling rate (°C/s), taken from the eutectic start (T_{ES}, being between the T_{Liq} and T_{ELow}) at 1 °C/s.

The most homogeneous microstructure is found to be the one with the highest T_{ELow} identified for 19 and 37 ppm B, as shown in Figure 6b,d. This was achieved despite a variation in the graphite count.

Figure 6 shows the highest measured graphite count obtained for the final two highest boron-containing melts but also the lowest measured value for smallest boron addition. Based on graphite count distribution, the graphite count appears to be more dispersed (higher standard deviation, SD), indicating a considerable graphite size variation. The higher SD is related to smaller flakes present locally and due to overall scatter by image analyses. In the case of 37 ppm B, this could partially be a result of the change from thin and fine D/E towards thicker A, which is also due to a higher *ACEL* value. Based solely on the achieved *ACEL*, it is assumed that inoculation efficiency or combined inoculation rate between the melts are not repeatable compared to the unmodified sample (0 ppm B).

3.6.2. FE-SEM

Using the backscattered electron detector (BSD) detector shown in Figure 7 and the undercooled FE-SEM microstructures, it is possible to observe the presence of primary carbo nitrides (white) composed of Ti, V and Mo, as well as their positions. In the last solidification region, carbides are more enhanced, confirming their non-equilibrium solidification nature. The dark phases are graphite inside the matrix (grey), showing mainly undercooled flake graphite (type D) with local interdendritic flake graphite (type E). Visually, carbides appear to increase with boron. However, measurements reveal that for boron values 0, 30 and 37 ppm B, there is a 0.64, 0.61 and 1.27 areal %, respectively. Therefore, there is no obvious difference in carbides, with an exception of those with the highest boron content.

An example of the location of the last solidification region is shown in Figure 8, where complex interactions with carbonitrides and non-metallic inclusions (MnS) are observed. Both complex carbonitrides and MnS are predicted by Thermo-Calc. The boron was not observed. Additionally, the pearlite (not shown here) did not reveal the presence of any boron.

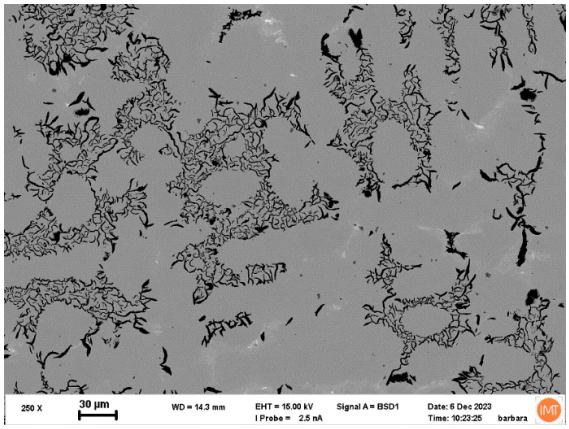

(**a**)

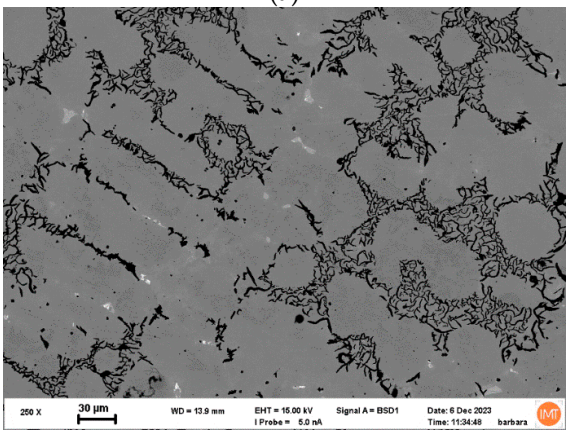

(**b**)

Figure 7. FE-SEM-BSD: an example of (**a**) reference sample with 0 ppm B; (**b**) 30 ppm B.

Based on the executed FE-SEM, it cannot be established whether or not boron-based nuclei were present in the last solidification region. It is recognised that BN should be ideal for graphite growth due to its hexagonality, but it is also recognised that boron has a limited oxygen affinity [13,23]. For example, boron, under highly oxidising conditions, can react with dissolved oxygen or by reducing less stable oxides than boron to form B_2O_3 type of oxides, while potentially also working as a nuclei for graphite, as it is hexagonal [42]. If considering B_2O_3, SiO_2, MgO and others (TiO, Ti_2O_3) as potential nuclei, B_2O_3 with approx. −320 kJ/mol (and others with <−320 kJ/mol) appears to be less stable based, on the Gibbs energy of formation per mole [O] in the desired temperature interval of 1145 °C and 1108 °C. However, the stability of B_2O_3 is close to SiO_2. It should also be added that B_2O_3 can thermodynamically interact (based on the Gibbs energy of reaction, ΔG_R) with other more stable oxides and form new (double) oxide products. For example, Ca is a commonplace additive for inoculation inside complex ferroalloys (i.e., FeSi) [43]. By interacting with oxygen, it forms a basic oxide, and by interacting with acids, boron oxide can potentially form CaB_xO_y. These or similar complexes in theory should at least partially remove boron from the residual melt and affect the nucleation potential as a cumulative effect. It is also recognised that oxide slags saturated with B_2O_3 can easily be reduced in steel containing Si [44], indicating that boron-related nucleation phenomena, if present, could fade with time. Limited boron saturation is expected inside oxides under a sufficiently high mass transfer rate of boron inside the melt into the boron-free oxide system (nuclei) and with sufficient time for saturation. The intensity of boron saturation in oxide-based nuclei and other oxides depends on the actual achieved distribution ratio of boron between oxides (nuclei) and the remaining melt (defined by L_B = wt.% B_{Oxide}/wt.% B_{Liquid}). This was not investigated in this study. However, the content of boron should remain practically unchanged during regular grey cast iron production, as melt refining in a metallurgical

sense is unwanted for grey cast iron to preserve sufficiently high nuclei density. The variation in distribution of boron between oxides and residual melt is found in some of the literature data [10,44].

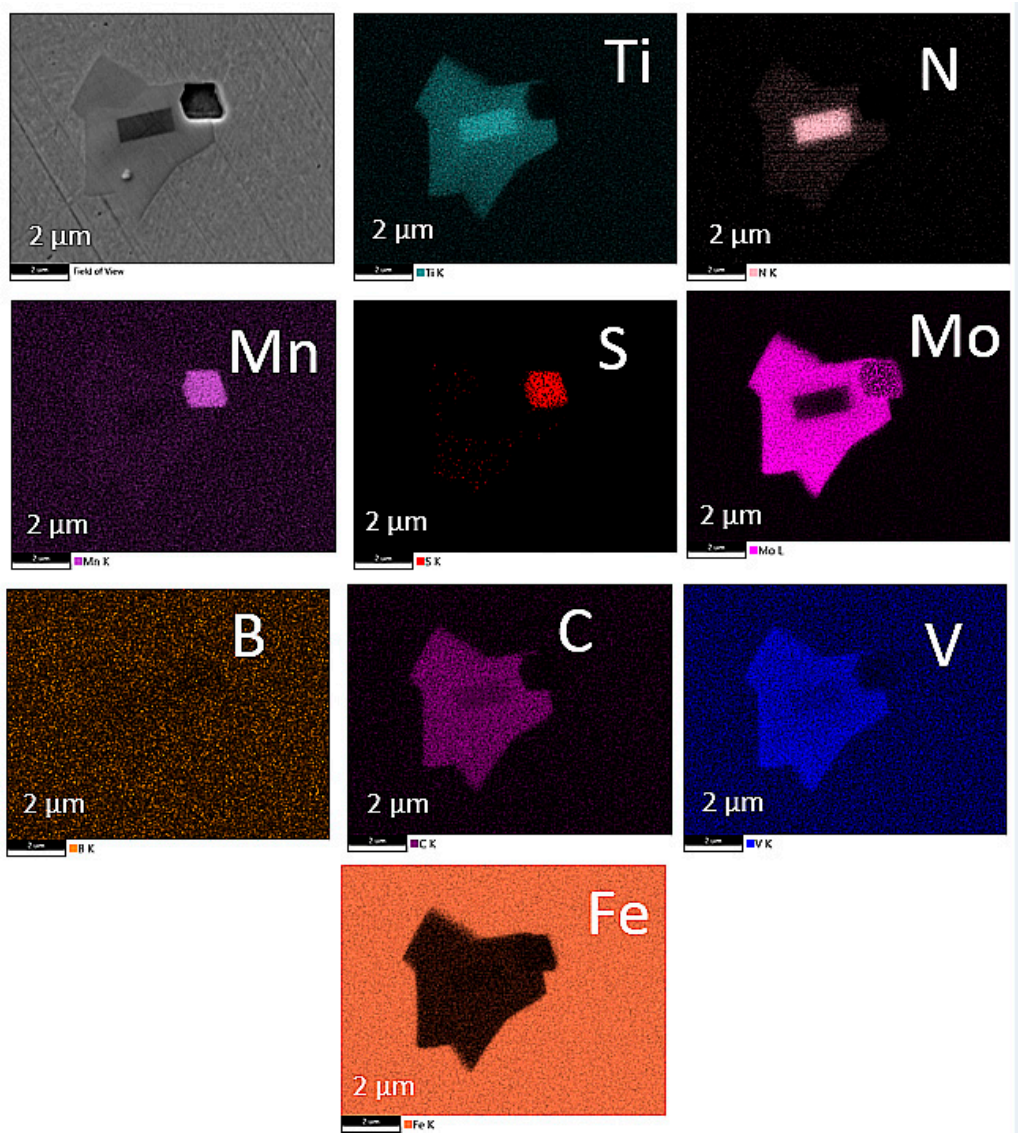

Figure 8. FE-SEM-EDS elemental distribution maps: these maps are calculated to show the actual element content (ZAF wt%), and not just signal intensity to avoid overlaps of B and Mo X-ray peaks. Sample: 37 ppm B.

3.7. Hardness at Slow Cooling Rates

Hardness as a function of the change of mechanical properties was tested for slow cooling rates, to evaluate whether or not there is a significant difference between the measured HB values of the TA samples (extracted adjacent to thermocouples) concerning boron by considering linearity. No linearity was observed ($r = -0.38$, $R^2 = 0.14$). However, by having a polynomial fit (of the second order), the regression model shows improved correlation (adjusted $R^2 = 0.68$), but is still rather weak in relation to R^2, where more than half of the data is represented well with the model, see Figure 9. However, the model is well-adjusted according to the p-value for dependent coefficients (B_i), by using test statistics with the ANOVA approach. This means that regression is sufficiently explained by the given model. The coefficients are given and explained further in the paper. The hardness scatter could be related to material homogeneity/heterogeneity observed after solidification and the related presence of graphite-free regions and changes in carbide percentage (areal.

%), as shown in Figures 6 and 7. This means that simple changes in the graphite count with boron is not the main cause of hardness variation but rather the achieved distribution of the soft ferritic regions. Based on [23,24], the excess of boron could stabilise pearlite and give the matrix a harder response. Increased primary carbides at slow cooling rates are potentially recognised in the last solidification front (according to FE-SEM) and the hardness jump for the highest values of boron could be the result of local coarse carbide formation. Based on the hardness response and the fact that boron is a ferrite stabiliser, an increased soft ferrite matrix could be the reason for the starting hardness drop [21]. A correlation between the addition of boron and the graphite count affecting the hardness was not correlated, as shown in Table 5.

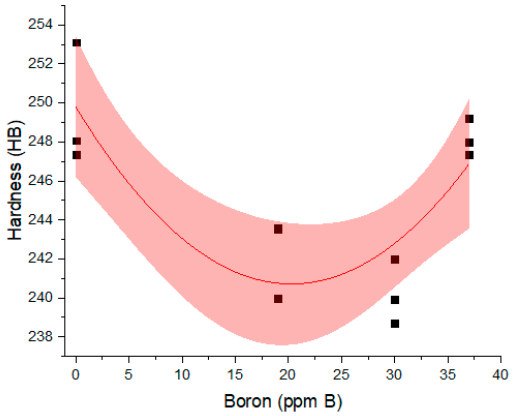

Figure 9. The hardness of TA extracted samples to evaluate the changes with the addition of boron with a 95% confidence band (red interval). The hardness is valid for 1 °C/s of solidification rate. No additional heat treatment (ferritisation) was performed.

Table 5. Pearson correlation coefficient, *r*, for boron sensibility test by actual towards predicted for correlation versus boron.

Correlation	Pearson Correlation Coefficient, *r*	*p*-Value (Level)	R^2	Significant
Liquidus (T_{Liq}) versus B	−0.69	0.3084	0.48	No
ACEL versus B	0.69	0.3084	0.48	No
ACEL versus GRF2	−0.85	0.1472	0.73	No
T_{ELow} versus B	0.65	0.3458	0.43	No
T_{EHigh} versus B	0.49	0.5091	0.24	No
T_{ES} versus B	0.50	0.5003	0.25	No
T_{sol} versus B	0.59	0.4101	0.35	No
Rec versus B	−0.98	0.0182	0.96	Yes
UQ versus B	0.97	0.0301	0.94	Yes
GRF2 versus B	−0.23	0.7734	0.05	No
S1 versus B	−0.43	0.5670	0.19	No
W versus B	−0, 96	0.0387	0.92	Yes
W versus *Rec*	0.96	0.0443	0.91	Yes
HB versus B	−0.38	0.6228	0.14	No
$T_{Pouring}$ versus W4	−0.92	0.0806	0.85	No
$T_{Pouring}$ versus HB	0.06	0.9403	0.00	No
Graph. count versus B	0.54	0.4558	0.29	No

Based on the small boron values, the presence of the measuring error for the boron also contributes to the scattered hardness relation with the boron for slow cooling rates of TA samples. Therefore, this relation of boron with hardness remains unclear. However, based on the overall results, a hardness drop was achieved compared to the reference (0 ppm B), despite local hardness jumps.

The equation for polynomial hardness fit with boron for slow cooling at 1 °C/s was fit using the equation:

$$y = Intercept + \sum B_i \cdot x^i; i = 1, 2, ... \quad (2)$$

where y is the predicted hardness, x represents the boron value in ppm and B_1 and B_2 are dependent and fitted coefficients. The starting hardness as an independent value is presented with $HB_{0\_ppm\_B}$. The final and simplest quadratic relation is given by:

$$HB = HB_{0\_ppm\_B} - 0.8941 \cdot boron\ (\text{ppm}) + 0.02204 \cdot boron^2\ (\text{ppm}) \quad (3)$$

The potential boron effect was considered using a factor W when considerable cooling rates are present. It is recognised that boron had a certain effect on *Rec*, as well as on W, which indicates the weak inoculation phenomena if the potential boron is not completely lost with time, as in the case of TA samples with slow melt cooling.

3.8. Correlation Probability

For all variables, the Pearson correlation coefficient, r, was calculated. The strength of relationships of measured values with boron varies from weak to strong linear correlation. Based on the results, it can be concluded that a strong linear relationship between two variables exists for *Rec*, related *UQ* and W with boron. This also goes with the coefficient of determination, R^2. Strong linearity was also observed between T_{Pouring} and $W4$ for intense cooling, but practically close to zero correlation for T_{Pouring} and measured hardness for slow cooling (TA cell). Additionally, inversed heat conductivity, GRF2, reveals a stronger linear correlation with ACEL than with boron, indicating the non-significance of the boron contribution to thermal conductivity change in this study.

The statistical significance of the Pearson correlation coefficient was tested where *Rec* and related *UQ*, as well as W, reveal that there is a statistically significant linear relationship. In the case of W versus *Rec*, the significance could also be a result of a third parameter. All other factors, including ACEL and T_{sol}, have a moderate or weak linear correlation; therefore, it can be concluded that the boron influence is rather weak for the studied concentrations.

Based on all analysed values, boron performs as a weak inoculant only under short hold and solidification times (wedge test). Based on linear regression an equation is set:

$$W4 = W4_{0\_ppm\_B} + (-0.21273) \cdot boron\ (\text{ppm}) \quad (4)$$

where a negative slope indicates a decreasing chill tendency for intense cooling rates with added boron, according to the laboratory settings. The influence of boron on recalescence is also described with a linear model, where $Rec_{0\_ppm\_B}$ represents recalescence measured for reference melt, without boron:

$$Boron\ influence\ on\ recalescence = Rec = Rec_{0\_ppm\_B} + (-0.058 \cdot boron\ (\text{ppm})) \quad (5)$$

Both *Rec* and $W4$ are well correlated, as shown in Table 5. It should be emphasised, that *Rec* changes with time, as its potential inoculation fades with time. Therefore, the equation above is set for the cooling/solidification rate of approx. 1 °C/s with the direct addition of boron. As the noise is rather high for Equation (5), the inoculation and/or change in recalescence phenomena cannot be considered solely as a part of boron, but it is assumed that other heterogeneous nuclei also contribute to this phenomenon.

Based on Table 5, that ACEL versus B and liquidus temperature versus B have the same Pearson correlation coefficient, as expected. This is due to calculation of ACEL directly from measured T_{Liq}.

4. Conclusions

Based on the conducted research, it was concluded that no very significant linear trend was observed at slow cooling rates of approx. 1 °C/s with the addition of boron for any of the measured parameters. The exception is that boron shows a significant decreasing effect in the recalescence (*Rec*) during eutectic graphite solidification on the temperature-time cooling curve. This is contrary to expectations. This indicates that boron could potentially affect graphite growth as short-term inoculation effect, meaning that boron can work as low-effective inoculator only. It is important to note that, based on the ATAS system, the boron effect was noticed even when it was almost negligible.

Graphite transformations from poor inoculated D to well inoculated A-type with boron at slow cooling rates was non-repeatable—the effect of boron is easily lost, and overall inoculation is dictated by ACEL.

At slow cooling rates, the effect of added boron concerning thermal conductivity observed indirectly by the GRF2 factor was recognised as non-significant under the condition of weak linear correlation. The inverted heat conductivity, GRF2, was more affected by the achieved ACEL than boron itself, because ACEL has a direct influence on the formed as-cast microstructure. The hardness at lower cooling rates was correlated with boron under the parabolic model showing the complex behaviour of the melts. An overall hardness decrease was observed with boron.

If bonded boron is present, a limited influence on the temperature interval between the stable and metastable eutectic is expected. There is no measurable effect of boron on nucleation of primary austenite.

The chill test for the increased solidification rates confirmed that the influence of boron was significant but not very significant. In the current study, the minor increasing graphitisation trend with boron is observed by the chill test only (short solidification times, fast cooling rates and the preservation of nucleation sites). This nucleation trend is also indicated by T_{sol} using TA at slower cooling rates, although it showed no distinctive trend.

Both TA and wedge chill test results reveal that boron, even in trace amounts, is influential and has very complex behaviour. The overall melt condition seems to be of higher importance than the actual achieved boron content, within the studied boron limits. None of the observed factors had a very significant response with boron up to 38 ppm B when using a linear regression model.

Boron can work as inoculator, which is consistent with some observations made and tests carried out by other authors.

Author Contributions: Conceptualisation, G.K. and J.B.; methodology, G.K. and J.B.; software, G.K. and U.K.; validation, G.K., U.K.; formal analysis, U.K, B.Š.B. and G.K.; investigation, G.K., U.K., B.Š.B. and J.B.; resources, G.K., J.B., B.Š.B., U.K. and A.R.; data curation, U.K.; writing—original draft preparation, G.K.; writing—review and editing, G.K., J.B., U.K., L.K., B.Š.B. and A.R.; visualisation, G.K.; All authors have read and agreed to the published version of the manuscript.

Funding: This research was funded by Republic of Slovenia and the European Union from the Recovery and Resilience Mechanism, NextGenerationEU.

Data Availability Statement: The data is unavailable due to privacy.

Acknowledgments: The authors would like to acknowledge industrial partner OMCO Metals Slovenia d.o.o. and Andrej Kump from Nova Cast, Sweden. The authors would also like to thank Luka Snoj, Anže Bajželj and Nejc Velikajne for their help with the experimental part. The authors acknowledge Financial resources for the project DigitKrom provided by the Republic of Slovenia (Spodbude za raziskovalno razvojne projekte NOO, 303-2-00109/2021/4) and the European Union from the Recovery and Resilience Mechanism, NextGenerationEU.

Conflicts of Interest: Author Andrej Resnik was employed by the company Omco Metals Slovenia d.o.o. The remaining authors declare that the research was conducted in the absence of any commercial or financial relationships that could be construed as a potential conflict of interest.

References

1. Stefanescu, D.M.; Alonso, G.; Larrañaga, P.; De la Fuente, E.; Suarez, R. Reexamination of crystal growth theory of graphite in iron-carbon alloys. *Acta Mater.* **2017**, *139*, 109–121. [CrossRef]
2. Tonkovič, M.P.; Mrvar, P.; Vončina, M.; Donik, Č.; Godec, M.; Petrič, M. Analysis and thermodynamic stability of nuclei in spheroidal graphite in Fe–C–Si alloys. *Mater. Tech.* **2021**, *55*, 533–539.
3. Sommerfeld, A.; Böttger, B.; Tonn, B. Graphite Nucleation in Cast Iron Melts Based on Solidification Experiments and Microstructure Simulation. *J. Mater. Sci. Technol.* **2008**, *24*, 3.
4. Alonso, G.; Larrañaga, P.; De la Fuente, E.; Stefanescu, D.M.; Natxiondo, A.; Suarez, R. Kinetics of nucleation and growth of graphite at different stages of solidification for spheroidal graphite iron. *Int. J. Met.* **2017**, *11*, 14–26. [CrossRef]
5. Stefan, E.; Chisamera, M.; Riposan, I.; Stan, S. Graphite nucleation sites in commercial grey cast irons. *Mater. Today Proc.* **2021**, *45*, 4091–4095. [CrossRef]
6. Campbell, J. The Structure of Cast Irons. *Mater. Sci. Forum* **2018**, *925*, 86–89. [CrossRef]
7. Taşşgin, Y.; Kaplan, M.; Yaz, M. Investigation of effects of boron additives and heat treatment on carbides and phase transition of highly alloyed duplex cast iron. *Mater. Des.* **2009**, *30*, 3174–3179. [CrossRef]
8. Zhang, J.; Yang, P.; Wang, R. Investigation of the Microstructures and Properties of B-Bearing High-Speed Alloy Steel. *Coatings* **2022**, *12*, 1650. [CrossRef]
9. Kolokoltsev, V.M.; Petrochenko, E.V.; Molochkova, O.S. Influence of boron modification and cooling conditions during solidification on structural and phase state of heat- and wear-resistant white cast iron. *CIS Iron Steel Rev.* **2018**, *15*, 11–15. [CrossRef]
10. Jakobsson, L.K. Distribution of Boron between Silicon and CaO-SiO_2, MgO-SiO_2, CaO-MgO-SiO_2 and CaO-Al_2O_3-SiO_2 Slags at 1600 °C. Ph.D. Thesis, Norwegian University of Science and Technology, Trondheim, Norway, November 2013.
11. Çolak, M.; Uslu, E.; Teke, Ç.; Şafak, F.; Erol, Ö.; Erol, Y.; Çoban, Y.; Yavuz, M. Investigation of the Effect of Solidification Time and Addition Amount of Inoculation on Microstructure and Hardness in Lamellar Graphite Cast Iron. *Arch. Foundry Eng.* **2022**, *22*, 24–33. [CrossRef]
12. Mendas, M.; Benayoun, S. Comparative study of abrasion via microindentation and microscratch tests of reinforced and unreinforced lamellar cast iron. *Friction* **2019**, *7*, 457–465. [CrossRef]
13. Zou, Y.; Ogawa, M.; Nakae, H. Interaction of Boron with Copper and Its Influence on Matrix of Spheroidal Graphite Cast Iron. *ISIJ Int.* **2012**, *52*, 505–509. [CrossRef]
14. Ha, J.S.; Hong, J.W.; Kim, J.W.; Han, S.B.; Choi, C.Y.; Song, H.J.; Jang, J.S.; Kim, D.Y.; Ko, D.C.; Yi, S.H.; et al. The Effect of Boron (B) on the Microstructure and Graphite Morphology of Spheroidal Graphite Cast Iron. *Materials* **2023**, *16*, 4225. [CrossRef] [PubMed]
15. Kasvayee, K.A.; Ciavatta, M.; Ghassemali, E.; Svensson, I.L.; Jarfors, A.E.W. Effect of Boron and Cross-Section Thickness on Microstructure and Mechanical Properties of Ductile Iron. *Mater. Sci. Forum* **2018**, *925*, 249–256. [CrossRef]
16. Bugten, A.V.; Michels, L.; Brurok, R.B.; Hartung, C.; Ott, E.; Vines, L.; Li, Y.; Arnberg, L.; Di Sabatino, M. The Role of Boron in Low Copper Spheroidal Graphite Irons. *Met. Mater. Trans. A* **2023**, *54*, 2023–2539. [CrossRef]
17. Eppich, R. Cast Iron Alloy Containing Boron. Patent: WO 2006/133355 A2, 8 June 2005.
18. Pawaskar, S.D. Effect of Boron in Cast Iron. Master's Thesis, Missouri University of Science and Technology, Rolla, MO, USA, September 2022. Available online: https://scholarsmine.mst.edu/masters_theses/8109 (accessed on 10 October 2023).
19. Krynitsky, A.I.; Stern, H. Effect of Boron on the Structure and Some Physical Properties of Plain Cast Irons. *J. Res. Natl. Bur. Stand.* **1949**, *42*, 465–479. [CrossRef]
20. Ankamma, K. Effect of Trace Elements (Boron and Lead) on the Properties of Gray Cast Iron. *J. Inst. Eng. Ser. D* **2014**, *95*, 19–26. [CrossRef]
21. Chen, X.; Li, Y.; Zhang, H. Microstructure and mechanical properties of high boron white cast iron with about 4 wt% chromium. *J. Mater. Sci.* **2011**, *46*, 957–963. [CrossRef]
22. Kanno, T.; You, Y.; Morinaka, M.; Nakae, H. Effect of Alloying Elements on Graphite and Cementite Eutectic Temperature of Cast Iron. *ISIJ Int.* **1998**, *70*, 465–470. [CrossRef]
23. Strande, K.; Tiedje, N.S.; Chen, M. A Contribution to the Understanding of the Combined Effect of Nitrogen and Boron in Grey Cast Iron. *Int. J. Met.* **2017**, *11*, 61–70. [CrossRef]
24. Röhrig, K. Einfluss von Legierungselementen auf die Eigenschaften von Gusseisen (G) Legiertes Gusseisen, Gusseisenwerkstoffe. *Gesserei-Prax.* **2019**, *4*, 21–26.
25. Persson, P.E.; Udroiu, A.; Vomacka, P.; Xiaojing, W.; Sjögren, T. ATAS as a tool for analyzing, stabilizing and optimizing the graphite precipitation in grey cast iron. In Proceedings of the 69th World Foundry Congress, FICMES, Hangzhou, China, 16–20 October 2010.
26. Thermal Analysis Cup. Available online: https://www.novacast.se/product/thermal-analysis-cup (accessed on 20 December 2023).
27. *ISO 6506-1:2005*; Metallic Materials-Brinell Hardness Test, Method 1: Test Method. ISO: Geneve, Switzerland, 2007.
28. *DIN ISO 945-1:2008*; Graphite Classification by Visual Analysisi, Part-1. ISO: Berlin, Germany, 2008.
29. *A367-11*; Standard Test Methods of Chill Testing of Cast Iron. ASTM International: Singapore, 2011.

30. Montgomery, D.C. *Design and Analysis of Experiments*, 8th ed.; Wiley: Hoboken, NJ, USA, 2013.
31. Pearson Correlation Coefficient: Formula, Examples. Available online: https://vitalflux.com/pearson-correlation-coefficient-statistical-significance/ (accessed on 20 December 2023).
32. Timelli, G.; Bonollo, F. Fluidity of aluminium die castings alloys. *Int. J. Cast. Met. Res.* **2007**, *20*, 304–311. [CrossRef]
33. Satir-Kolorz, A.H.; Feichtinger, H.K. On the solubility of nitrogen in liquid iron and steel alloys using elevated pressure. *Int. J. Mat. Res.* **1991**, *82*, 689–697. [CrossRef]
34. Sigworth, G.K.; Elliot, J.F. The Thermodynamics of Liquid Dilute Iron Alloys. *Met. Sci.* **1974**, *8*, 298–310. [CrossRef]
35. Hultgren, R.; Desai, P.D.; Hawkins, D.T.; Gleiser, M.; Kelley, K.K. *Selected Values of the Thermodynamic Properties of Binary Alloys*; American Society for Metals: Metals Park, OH, USA, 1975.
36. Naraghi, R.; Selleby, M.; Ågren, J. Thermodynamic of stable and metastable structures in Fe-C system. *Calphad* **2014**, *46*, 148–158. [CrossRef]
37. Banya, S.; Matoba, S. Activity of carbon and oxygen in liquid iron. *Tetsu-Hagane Overseas* **1963**, *3*, 21–28. [CrossRef]
38. Stefanescu, D.M. *Thermodynamic Properties of Iron-Base Alloys*; ASM Handbook Committee: 1988; ASM International: Metals Park, OH, USA, 1988; Volume 15.
39. Stefanescu, D.M.; Suarez, R.; Kim, S.B. 90 years of thermal analysisi as a control tool in the melting of cast iron. *China Foundry* **2020**, *17*, 69–84. [CrossRef]
40. Holmgren, D.; Diószegi, A.; Svensson, I.L. Effects of Inoculation and Solidification Rate on the Thermal Conductivity of Grey Cast Iron. *Giessereiforschung* **2006**, *58*, 12–17.
41. Thermal Analysis of Cast Iron, Heraeus Electro-Ni. Available online: https://www.heraeus.com/media/media/hen/media_hen/products_hen/iron/thermal_analysis_of_cast_iron.pdf (accessed on 15 December 2023).
42. Sato, A.; Aragane, G.; Ogata, S.; Yamada, K.; Yoshimatsu, S. A method of Recovery of Boron from Fig Iron and Boron Oxide from Slag. *Trans. Iron Steel Inst. Jpn.* **1986**, *26*, 949–954. [CrossRef]
43. TDR, Product Line Overview. Available online: http://www.tdrlegure.si/files/pdf/Katalog-2019-ARR.pdf (accessed on 15 June 2023).
44. Sychev, A.V.; Salina, V.A.; Babenko, A.A.; Zhuchkov, V.I. Distribution of Boron between Oxide Slag and Steel. *Steel Transl.* **2017**, *47*, 105–107. [CrossRef]